**Title:**

**Reverberations, coda waves and ambient noise: correlations at the global scale and retrieval of the deep phases**

**Authors:**

P. Boué*, P. Poli, M. Campillo, P. Roux

**Corresponding author (*):**

**pierre.boue@ujf-grenoble.fr**

**Phone: +33 (0)4 76 63 52 39**

**Affiliation:**

Institut des Sciences de la Terre

Université Joseph Fourier and CNRS

Grenoble, France

**Summary:**

Cross-correlation of continuous broadband records allows the retrieval of body waves at teleseismic distances. These continuous records mainly contain low-amplitude background noise that comes from ocean–crust interactions, although there are also many transient events of different magnitudes and their coda associated with reverberation and/or scattering. We present an analysis at the global scale of these different contributions in the context of body-wave retrieval using the cross-correlation technique. Specifically, we compare the correlation of long codas after strong earthquakes with those of the quietest days. In the long period range (25-100 s), several phases that propagate in the deep Earth are observed in the correlations of the signals recorded after earthquakes, with some of these phases showing non-physical polarization. At the same time, the global section of correlations shows a series of spurious branches. These features are reproduced with synthetic correlations. A stack of the quietest days of the year shows that body waves are still present, with relative amplitudes that are closer to those expected for the actual Earth response. When considering shorter periods (5-10 s), the reconstruction of the deep phases is not affected by the earthquake coda, due the dominance of scattering over reverberation.

**Key words:** Interferometry, Body waves, Global scale

**Main Body:**

## 1 Introduction

From the regional to the global scale, ambient seismic noise primarily refers to the wavefield that is continuously produced by the interactions of the fluid envelopes, as mainly through ocean waves, and the solid Earth. The source mechanisms of these interactions is frequency dependent. Short-period noise (4 s to 30 s) is dominated by the two microseism peaks (e.g., Longuet-Higgins, 1950; Ardhuin et al., 2011). At longer periods (above 30 s), other mechanisms take place, which are also known as Earth hum (Kedar and Webb, 2005), such as the proposed shear-wave generation by infragravity waves (Fukao et al., 2010). Here the term “noise” is defined through its difference from the earthquake records. The duration of an earthquake record is defined with respect to a particular signal-to-noise ratio (SNR) threshold, and it varies with frequency for a given event magnitude. Furthermore, depending on the frequency, the scattering strength governs the ratio between the randomly scattered waves and the ballistic waves that reverberate between the main boundaries (i.e., the Earth surface, the core-mantle boundary).

It has been demonstrated that the elastic response between two stations can be evaluated by correlation of the records of scattered waves (Campillo and

63 Paul, 2003) or long ambient noise records (Shapiro and Campillo, 2004). As
64 expected from the theoretical Green's function between two points at the
65 free surface, the correlations of continuous records are dominated by surface
66 waves. The application of this approach has led to numerous examples of
67 surface-wave imaging (e.g. Shapiro et al., 2005; Sabra et al., 2005a;
68 Ritzwoller et al., 2011). The extension of the approach to body waves is
69 indeed appealing, although the level of the remaining random fluctuations in
70 the correlations makes the identification and exploitation of weak signals
71 difficult. Furthermore, the sources of ambient noise are likely located at the
72 surface, which results in a dominance of surface waves in the noise records.
73 However, teleseismic body-waves have been observed in noise records (e.g.
74 Vinnik, 1973; Gerstoft et al., 2008; Landès et al., 2010). The search for body
75 waves in the correlations has been successful in the last few years, which
76 started with the crustal phases (Zhan et al., 2010; Ruigrok et al., 2011; Poli et
77 al., 2012a). Then, deep vertical reflections were detected from the mantle
78 transition zone (Poli et al., 2012b) and from the core (Lin et al., 2013), with
79 data from regional arrays. The complete teleseismic section was
80 reconstructed by cross-correlation using a worldwide combination of arrays at
81 short to long periods (5 s to 100 s; Boué et al., 2013) and at long to very long
82 periods (30 s to 300 s; Nishida, 2013). These last studies demonstrated the
83 feasibility of ambient noise body-wave imaging. Lin and Tsai (2013) also
84 discussed core-phase retrievals using antipodal station pairs.

Different processing has been used in all of these studies, and especially regarding the removal of transient signals. Nishida (2013) applied the most rigorous processing, using the Global Centroid Moment Tensor catalog (Ekström et al., 2012) to systematically remove long time windows corresponding to earthquakes and the following few days, the number of which depended on the event magnitude (Nishida and Kobayashi, 1999). Lin et al. (2013) and Boué et al. (2013) used less restrictive criteria. At the global scale, both Nishida (2013) and Boué et al. (2013) observed mantle body waves but obtained different results for the amplitudes of the core phases, which are weaker, and were more realistic in the correlation computed by Nishida (2013). Note that large-amplitude core phases were also reported by Lin et al. (2013).

Boué et al. (2013) questioned the relevance of these high-amplitude phases, and suggested that they show non-physical features. By non-physical, we mean here that these features do not appear in the natural Green's function. For example, the phase in the correlation corresponding to ScS is observed at short distances with strong amplitudes for the vertical component, which leads to an obvious problem of polarization. The presence of spurious arrivals in the correlation section challenges the applicability of noise imaging to body-wave problems in the deep Earth. We address this problem here, by

analyzing the conditions under which reliable information can be extracted from noise correlations.

On the other hand, Lin et al. (2013) observed a strong correlation between the phases that reach the deepest parts of the Earth (ScS, P'P'df) and the seismicity. They suggested that earthquakes mainly excite these body waves. Finally the observations of Lin et al. (2013) and Boué et al. (2013) included spurious phases that are not in the Earth response, or at least, have different relative amplitudes. The problem of spurious arrivals due to multiples was discussed on a smaller scale by Snieder et al. (2006). Concerning wave propagation at the global scale, Ruigrok et al. (2008) discussed the imperfect reconstruction of the Green's function from surface source records, which reveals the presence of spurious arrivals (ghost events). They derived an elastodynamic relation from the representation theorem showing that knowledge of the responses of the medium with and without the effects of the free surface is required to retrieve the exact Green's function. They verified this theoretical statement numerically with acoustic simulations.

By investigating the temporal evolution of the reconstructed Green's function after large seismic events, it is shown in the present study that the processing used can explain these observations at long periods. The structure of this report is the following. First, the dataset used and the

129 processing applied are shown. Then we compare the quality of the
130 reconstruction of some of the phases with the seismicity and the microseism
131 excitation over a whole year. We present a synthetic example of the
132 reconstruction of partial Green's functions using a simulated long time
133 reverberated coda wavefield to explain the characteristics of spurious
134 arrivals. Finally, the study focuses on the particular propagation geometry
135 between Finland and Japan.
136
137
138 **2 Data and processing**
139 In this study, one year was selected (2008) for the vertical-component
140 records from a set of 420 stations distributed worldwide (Figure 1). The BH
141 channels are used after removal of the instrumental response, and
142 decimation to a 5-Hz sampling frequency. Note that some of these stations
143 are not available during the whole of the year period. All of the networks
144 involved are detailed in the Appendix. The continuous records were
145 processed similarly to Boué et al. (2013), which includes spectral
146 normalization of the noise traces (whitening). Cross-correlations are
147 computed for 4-h time windows, with a correlation lag of 4000 s, and
148 normalized through the square root of the energy of both of the traces. They
149 are directly stacked over one day, in the 5 s to 100 s period band. With this
150 processing, we can detect and choose to remove the 4-h time window that

151 contain ballistic arrivals of strong transient events (Boué et al., 2013). At the
152 same time, the scattered and reverberated coda waves from earthquakes are
153 retained. Eventually, the dataset contained more than 80 000 correlations
154 per day, which corresponds to each possible station pair. These correlations
155 can then be stacked either over a given period (e.g., days, weeks), which
156 results in one correlation per station pair, or over space, which results to one
157 correlation for a given average distance (bin) per day. The combination of
158 both stacks corresponds to the global section, for which correlations are
159 sorted as a function of distance from 0° to 180° with a bin size of 0.1°, and
160 stacked over the year. This is shown in Figure 2b, as the resulting vertical–
161 vertical correlations, which represent the global average propagation. It is
162 therefore justified to compare this with the synthetic Green's function
163 computed in a spherical Earth using the Preliminary Reference Earth Model
164 (Dziewonski and Anderson, 1981). Figure 2a shows the synthetic
165 seismograms computed using the spectral element method (Nissen-Meyer et
166 al., 2007, 2008). We simulate a simple vertical point force with a Gaussian-
167 shaped dominant period of 40 s. Although we note a general visual
168 agreement that indicates that numerous deep phases are emerging from the
169 correlation, there are some noticeable discrepancies, some of which have
170 non-physical characteristics. The comparison between Figure 2a and 2b
171 should remain qualitative, as the 3D Earth structure favors the emergence of
172 some phases after the spatial stack on the real data section (Figure 2b). For

example, Rayleigh waves can stack destructively, particularly at short periods, due to heterogeneities in shallow structures of the Earth.

In the global correlation section, some arrivals are present before the direct P-wave (Figure 2b). As already noted, the ScS phase has a too high relative amplitude. Even if the section representation with correlations stacked over distance bins enhances small move-out phases with a more constructive stack compared to large move-out phases like Rayleigh waves, it remains that ScS should not be visible on a vertical-component section at a distance close to 0°. Other deep phases, such as PKP and P'P'df, have high amplitudes relatively to the mantle, or even to the Rayleigh wave. Finally, there are some low-frequency spurious arrivals between the ScS and the P'P'df. In the following, we study how reverberated waves that follow large earthquakes affect the correlations. As the daily correlation for a given pair does not show a sufficient SNR, it is necessary to stack the correlations over space to produce the daily reconstructed signals. In practice we consider bins of 0.1° for the spatial average.

## 3 Contributions to correlations

We construct daily global sections that are used to evaluate the temporal evolution of the contributions of the daily correlations to the reconstructed

195 Green’s function. The daily contributions are quantified by computing the
196 coherence between the daily and yearly reconstructions in specific time–
197 distance domains. We selected six different time–space domains that
198 correspond to different phases (Figure 2b, colored boxes), and processed the
199 image correlation for the 366 days of the year. This processing was
200 performed with sections that had been filtered in the short period (5-10 s)
201 and long period (25-100 s) ranges. The data are shown in Figure 3. High
202 coherence means strong excitation of the given phase for a given day. These
203 coherences are compared to the daily seismicity (Figure 3a) and oceanic
204 secondary microseism excitation (Figure 3b) from Hillers et al. (2012). The
205 daily cumulative seismic moment is computed from the International
206 Seimological Centre catalog after the selection of events with a magnitude
207 >4. Ocean excitation for the secondary microseism includes bathymetric
208 effects (Longuet-Higgins, 1950), and this is integrated over the whole ocean
209 surface.
210
211 At short period, P and PcP are well reconstructed, as shown in Figure 2c. The
212 daily coherence of these two phases (Figure 3c) is independent of the
213 seismicity rate. This indicates the efficiency of the initial processing that
214 included the removal of large earthquakes for this period range. There is also
215 no clear relationship between the time-dependent coherence of the
216 reconstructed waves and the amplitude of the secondary microseism

217 excitation, even if this excitation varies by two orders of magnitude. This
218 indicates that after the normalization of the correlations, their properties are
219 independent of the amplitude of the ocean excitation, which is probably due
220 to its complex spatial and temporal source pattern. Globally, the coherence
221 appears stationary through the year. We interpret this point as the signature
222 of the inherently complex nature of the short-period ambient noise with a
223 significant contribution of scattered waves.
224
225 A different picture is drawn from the results for long-period correlations. The
226 main feature shown in Figure 3d is the strong correlation of the main deep
227 phases with seismicity. In the 25-s to 100-s period band, the main deep
228 phases, such as ScS and P’P’df, and also PcP and PKP, are strongly correlated
229 to seismicity. This is shown by the high amplitude peaks of the daily
230 coherence for the large earthquakes, as also highlighted by the gray vertical
231 lines in Figure 3d. A similar observation was made by Lin et al. (2013) and Lin
232 and Tsai (2013) for regional and antipodal propagations respectively. For the
233 mantle P-waves and S-waves, no such strong correlation with seismicity is
234 observed. However a correlation is observed for a series of events in
235 February. These high-coherence peaks are not coincident with the strong
236 maxima of the core phases. Some smaller peaks for the S-SS phases are not
237 correlated with any strong earthquakes, as for example in May or November.
238 This suggests another source contribution for these S-waves at long periods,

239 which might be associated with the coupling of ocean infra-gravity waves
240 with the seabed topography, as proposed by Fukao et al. (2010).
241 Furthermore, some coherence peaks are extended to the days after the
242 earthquake. This illustrates the importance of the long-standing
243 reverberations following large magnitude events. Note that even in the case
244 of the largest event in the year 2008, the May 12 Mw 7.9 Sichuan
245 earthquake, the high coherence period does not exceed 2 days after the
246 mainshock.
247
248 The value of the coherence is difficult to analyze, as it depends on the
249 source–receiver geometry, focal mechanism, and receiver–receiver geometry.
250 We observe that large earthquakes do not always lead to high coherence
251 peaks. The correlation with seismicity is nevertheless obvious for deep
252 phases. In the following, we isolate the contributions of earthquakes to the
253 global correlations, and we analyze their part in the emergence of spurious
254 arrivals or anomalous polarizations. This will lead to modified processing for
255 long-period correlations.
256
257 **4 Long-period processing**
258 Using the long-period band, the coherence is presented in Figure 3d, where
259 we define high-coherence days (HCDs) by selecting the days with high
260 seismic activity that are also associated with high coherence for each phase.

In practice, we selected days with a coherence >0.2 and with a corresponding local maximum in the cumulative seismic moment function. For the mantle P-waves and S-waves, this results in selecting a group of days that correspond to the high-amplitude peaks in February and March. For the deep reflected waves, a criterion based on the average fluctuations of the coherence is used to detect the local maxima. In the end, 30 days are considered as HCDs. The remaining days of the year are considered as low-coherence days (LCDs). We now compare the teleseismic correlation sections built from these subsets.

Correlations that correspond to LCD and HCD subsets are stacked, to get two global sections; these sections are shown in Figure 4a and b, respectively. A comparison of these two sections shows that the spurious phases that are visible on the global section of Figure 2b are related to the HCDs, and thus to the strong seismic activity. Figure 4a (for the LCDs) shows a lower SNR than the year stack (Figure 2b), although no spurious arrivals are visible and the relative amplitudes of the different phases fit the theoretical Green's function better, which is also shown in Figure 4c. The section for LCDs is close to the data of Nishida (2013), but here only for a 336-day stack.

On the other hand, spurious arrivals (as previously described) are illustrated in Figure 4b. With the relatively low amplitude of the Rayleigh wave, there is

283 a spurious arrival with a negative move-out between 0° to 20° and for times
284 <5 min. Spurious phases arrive ahead of the P-wave. This HCD section also
285 shows abnormally high relative amplitudes for phases, such as for ScS, PKP
286 and P'P'df. The previous observations suggested that the HCD section is
287 dominated by correlation cross-terms between the various reverberated
288 waves that continue for tens of hours after a large earthquake. This is a
289 variant of the process of emergence of spurious arrivals that was described
290 by Snieder et al. (2006).
291
292 The anomalous amplitudes appear for phases with very small move-out (i.e.,
293 very large apparent velocity). In the absence of a significant scattering at
294 long periods, we postulate that the strong contributions for the reflections in
295 the correlations are generated by multiple reflections. These multiple deep
296 reflections have large Fresnel zones, which means that the region in which a
297 source contributes is also very large. A source that is not along an eigenray
298 joining the two stations, but in a wide Fresnel zone, nevertheless has a
299 contribution. This can result in incorrect delays in the arrival times, and also
300 potentially in polarization anomalies. To test this hypothesis, a synthetic
301 example of a global scale cross-correlation was computed. This experiment
302 simulates the contributions of impulsive sources to the correlations. A vertical
303 point force is applied at the surface of a spherical model (PREM) which
304 includes attenuation. The wavefield is computed for a propagation duration of

2 days and recorded at numerous positions at the Earth surface. As the problem is axis symmetric, the computation can be restricted to receiver points on a great circle. We apply the same cross-correlation processing to the 2-day-long synthetics as for the real data. The resulting correlations are sorted by distance between the sensors and are stacked for all available source positions. Using the reciprocity theorem, this simulation is equivalent to having sources everywhere on the Earth surface and to the computing of the resulting cross-correlation for any sensor combination. The synthetic section is shown in Figure 4d. The main phases of the Earth Green's function are reconstructed. The anomalous characteristics that have been observed in the HCD section (Figure 4b) are visible: strong amplitudes of deep reflected waves with flat move-out, a spurious arrival before the P-wave arrival-time, and the inverse move-out phase in the range 0-20° and 0-5 min. This excellent qualitative agreement shows that anomalous phases in the correlations are produced by the coherent impulsive earthquake sources. This analysis was carried out for a global distribution of sources and stations. To go further in the understanding of the retrieved body waves at the global scale, we have to focus on a specific geometry; i.e., a specific travel path, to evaluate the impact of localized sources.

## 5 A specific geometry: the FNET-LAPNET dataset

The FNET (Japan) and LAPNET (Finland) arrays were selected (Figure 5, blue triangles), as they are both dense (*ca*. 40 stations) and with relatively small apertures compare to their relative distance (*ca*. 63°). We first repeat the processing of the selection of HCDs and LCDs for this selected dataset. The comparisons between correlations stacked for the whole year for the HCDs and the LCDs are shown in Figure 6. Specifically, we focus on S, SS and P'P'df waves at long period (Figure 6a-c), and on the P and PcP waves at short period (Figure 6d-f). The mantle P-wave at the long period is too weak to be visible on this section representation. Figure 6b shows that P'P'df is dominant for HCDs. Also, we can see lower amplitude flat move-out spurious arrivals due to correlation cross-terms from multiple reverberations. The Rayleigh wave, and also the S and SS waves are reconstructed in the stacking of the LCD. At shorter period, Figure 3 shows that the P and PcP waves in the noise correlations are not associated with coherent contributions of earthquakes. These two waves are well retrieved in the LCD stack. Figure 6 shows the theoretical arrival times for PREM (Figure 6, red lines), which confirm the phase identifications and indicate qualitative agreement even for the P'P'df phase, with an anomalous amplitude relatively to other phases at long periods.

To analyze the time accuracy of the different reconstructed phases, we performed slant stacks based on the theoretical travel-time curves (PREM).

These data are presented in Figure 7, where the travel-time obtained for all of the year, the HCD stack and the LCD stack are compared. At short period, there is no significant phase shift between the stacks for the P (Figure 7a) and PcP (Figure 7b) phases. The LCD stack gives a better SNR than the HCD stack, with a much stronger emergence of the signal. The SNR is expected to be directly related to the square root of the duration of the time series, which have been correlated (Sabra et al., 2005c; Larose et al., 2008). Here, this effect accounts for a factor about 3.5 in favor of the LCD. This is similar to our observations. This indicates that there is no specific effect of reverberated short-period waves after a few hours following an earthquake. This supports the pertinence of the processing, and the origin of the correlations in the waves continuously generated by the oceanic gravity waves, especially in the frequency bandwidth corresponding to secondary microseisms.

At longer period, the S-wave (Figure 6c) is only visible on the LCD. The SS-wave (Figure 7d) does not emerge from the slant stack, even if it appears to be visible in Figure 6. Finally, the P'P'df phase (Figure 7e) is visible on both the LCDs and HCDs, with a better SNR on the HCD stack, as seen in Figure 6. The two waveforms, both of which are filtered in the 25-100 s period band, show different dominant periods according to their corresponding sources. The HCD trace is dominated by longer period waves, coming from earthquakes, than those of the LCD trace. We measured a significant time

370 shift at a 50 s central period, of about 4.5 s. This difference can suggest a
371 shift associated with unevenly distributed noise sources at the Earth surface,
372 similar to the 2D effect discussed in 2D by Froment et al. (2010).
373
374 To study the potential effects associated with source geometry, we
375 reproduced the coherence analysis of Figure 3 but limiting the analysis to the
376 FNET to LAPNET paths. The results are presented in Figure 8. Daily
377 cumulative seismic moment and secondary microseism excitation from the
378 ocean are also reported for comparison.
379
380 At shorter period, there is still no clear correlation between phase coherence
381 and seismic activity or microseism excitation. To be more specific, we
382 evaluated the microseism in the region where it is expected to contribute
383 coherently to the correlations. We define these geographical areas (lobes) as
384 the Fresnel zones on the Earth surface of the first two bounces of the P-waves
385 (Figure 5). These so-called endfire lobes were described by Sabra et al.
386 (2005b) for an oceanic waveguide. On the assumption of a radial velocity
387 model (no lateral heterogeneities), all of these lobes are located along the
388 great circle joining the two arrays, and their radius increases for each
389 successive bounce. Even with this processing, there is no observation of any
390 clear relationship between microseism excitation and specific event in the
391 daily coherence series. The exact origin of the short period signals observed

remains unclear. Nevertheless, this can indicate that the coherence is probably more controlled by the large-scale spatial distribution of the sources than by the amplitude of specific events, as expected for the contribution of scattered waves. This is illustrated in Figure 8c, where there is a slight seasonal trend with higher amplitude during the northern hemisphere summer. This might be related to the location of the endfire lobes, as mainly in the southern hemisphere, where the excitation is dominant during the northern hemisphere summer (Landès et al., 2010).

At long periods, the effect of scattering as large as for the short period is not expected. We have shown also the importance of the long-standing multiple reflections, that we refer to as reverberations. For the long period range, Figure 8d shows a smaller number of coherence peaks than in Figure 3, for the entire set of station-to-station paths. This indicates a selective geometrical effect. The main coherence peaks observed for the FNET-LAPNET paths are still correlated to seismic activity. This is particularly true for the P'P'df phase. Mantle P-waves and S-waves do not show such strong correlations with seismicity. The P'P'df phase, which has the larger coherence peaks, is used to define the set of days that were associated with strong contributions to the correlations. The epicenters of the large events that occurred on these days are shown in Figure 5 (yellow stars). Note the absence among these events of the largest earthquake of the year, namely

414 the May 8, 2008, Sichuan earthquake. A group of events is located along the
415 great circle that joins the centers of the networks (Figure 5, white). Event 4a
416 shown in Figure 5 is located far from the great circle, but we cannot
417 distinguish its influence with respect to event 4b, which occurred the same
418 day and was located on the great circle. Events 2 and 5 (Figure 5) were
419 selected, although they do not belong to the great circle. These last events
420 are deep earthquakes (>500 km), and they produced a coherence peak only
421 for P'P'df.
422 Finally, the time accuracy of the P'P'df phase is evaluated at long period as a
423 function of the location of sources for HCDs. Figure 9 shows the slant stack of
424 P'P'df for all of the correlations of the two arrays, but only for the days
425 corresponding to events 1 and 2, respectively. Even if both of these
426 waveforms show similar shapes, their envelopes reveal a clearly different
427 arrival-time. The P'P'df phase that was reconstructed from event 2 (out of the
428 great circle between the two array centers), arrived several seconds before
429 the PREM theoretical time. This is not the case for event 1, which was aligned
430 with the two arrays, and so might better contribute to the Green's
431 reconstruction. Phase shift analysis reveals a 2 s delay at a 50 s central
432 period. Even if this time delay is smaller than that observed using envelopes,
433 this is a good indication that the use of correlations of multiple reflections
434 from large earthquakes should be used with caution for travel-time
435 measurements.

436

437 **6 Conclusions**

438 Nishida (2013) and Boué et al. (2013) showed that the global scale
439 propagation of body waves can be retrieved by cross-correlation of
440 continuous records. The conditions of the reconstruction of the deep body
441 phases are different for the period band considered here. Two elements are to
442 be considered: the nature of the excitation, and the part of the scattering
443 associated to wave propagation.

444

445 The relation between seismicity and deep phase reconstructions at long
446 period (25-100 s) is illustrated here on the global scale, as it was performed
447 at short distances by Lin et al. (2013) and for antipodal station pairs by Lin
448 and Tsai (2013). This is particularly clear for core reflected and transmitted
449 phases, but not very clear for P and S mantle phases. Also, these
450 reconstructed signals show amplitude and polarization anomalies. We
451 reproduced the main spurious patterns with synthetic seismograms and their
452 correlations. These spurious arrivals correspond to correlations between
453 various coherent phases that are generated by earthquakes, although they
454 are not strictly part of the physical Green's function. These discrepancies are
455 theoretically expected from the analysis of the reconstruction of the Green's
456 function based on the representation theorem proposed by Ruigrok et al.
457 (2008). With the removal of the coherent earthquake wavefield from the

458 dataset, which can last several days for large events, we obtain correlations
459 of ambient noise that are closer to the theoretical Green's function and
460 exempt of spurious phases. At shorter period (5-10 s), the reconstructed
461 phases are not correlated with seismicity, which is probably due to the
462 prominence of scattering over reverberation. No clear correlation was found
463 between the phase reconstruction and the microseism excitation amplitude.
464 This is what we would expect as the effect of the correlation processing
465 combined with the nature of the source excitation, which is a spatially
466 extended uncorrelated continuous source. The difference in the behavior
467 between scattered short-period waves and reverberated long-period waves is
468 explained because the scattering enhanced the directional diversity of the
469 waves. Ideally, the correlation of scattered waves leads to the exact Green's
470 function (Campillo and Paul, 2003). In contrast, in spite of their long duration,
471 the long-period reverberations locally conserve a narrow directionality. These
472 behaviors were formulated mathematically by Garnier and Papanicolaou
473 (2009, 2012). At long periods, with the scattering being weaker, the effect on
474 the correlations is not expected to be as strong as at short periods.
475
476 Finally, a particular receiver geometry was chosen (LAPNET-FNET) to study
477 the effects of the source location with respect to the areas of constructive
478 contributions. The earthquakes that contribute to high daily coherence are
479 mainly aligned with station-to-station direction. Nevertheless, an example of

a clear travel-time bias on the P’P’df phase is shown for a single event with high coherence. Particular care has therefore to be taken at the long period to remove long coherent reverberated waves, for the recovery of the natural Earth elastic response with useful accuracy.

**Acknowledgments**

This study was supported by the European Research Council through the advanced grant Whisper・227507. All of the data used in this study were obtained through the IRIS, NIED and RESIF data centers. We used data from numerous seismic networks, and we thank all of the dedicated seismologists and technical staff who run these networks for making their seismic data available. Finally the authors thank Kees Wapenaar and an anonymous reviewer for their careful review and constructive comments that helped in improving this manuscript.

**References:**

F. Ardhuin, E. Stutzmann, M. Schimmel, and A. Mangeney. Ocean wave sources of seismic noise. Journal of Geophysical Research: Oceans, 116(C9): n/a–n/a, 2011. ISSN 2156-2202. doi: 10.1029/2011JC006952.

P. Boué, P. Poli, M. Campillo, H. Pedersen, X. Briand, and P. Roux. Teleseismic correlations of ambient seismic noise for deep global imaging of the earth. Geophysical Journal International, 194(2):844–848, 2013. doi: 10.1093/gji/ggt160.

M. Campillo and A. Paul. Long-range correlations in the diffuse seismic coda. Science, 299(5606) :547–549, 2003. doi: 10.1126/science.1078551.

A. M. Dziewonski and D. L. Anderson. Preliminary reference earth model. Physics of the Earth and Planetary Interiors, 25(4):297–356, 1981. ISSN 0031-9201. doi: 10.1016/0031-9201(81)90046-7.

G. Ekström, M. Nettles, and A. Dziewoński. The global CMT project 2004–2010: Centroid-moment tensors for 13,017 earthquakes. Physics of the Earth and Planetary Interiors, 200–201(0):1–9, 2012. ISSN 0031-9201. doi: http://dx.doi.org/10.1016/j.pepi.2012.04.002.

B. Froment, M. Campillo, P. Roux, P. Gouédard, A. Verdel, and R. L. Weaver. Estimation of the effect of nonisotropically distributed energy on the apparent arrival time in correlations. Geophysics, 75(5):SA85–SA93, 2010. doi: 10.1190/1.3483102.

Y. Fukao, K. Nishida, and N. Kobayashi. Seafloor topography, ocean infragravity waves, and background love and rayleigh waves. Journal of Geophysical Research : Solid Earth, 115(B4):n/a–n/a, 2010. ISSN 2156-2202. doi: 10.1029/2009JB006678.

J. Garnier and G. Papanicolaou. Passive sensor imaging using cross correlations of noisy signals in a scattering medium. SIAM Journal on Imaging Sciences, 2(2):396–437, 2009. doi: 10.1137/080723454.

J. Garnier and G. Papanicolaou. Correlation-based virtual source imaging in strongly scattering random media. Inverse Problems, 28(7):075002, 2012.

P. Gerstoft, P. M. Shearer, N. Harmon, and J. Zhang. Global p, pp, and pkp wave microseisms observed from distant storms. Geophysical Research Letters, 35(23):n/a–n/a, 2008. ISSN 1944-8007. doi: 10.1029/2008GL036111.

G. Hillers, N. Graham, M. Campillo, S. Kedar, M. Landès, and N. Shapiro.

539 Global oceanic microseism sources as seen by seismic arrays and predicted
540 by wave action models. Geochemistry Geophysics Geosystems, 13:Q01021,
541 2012. doi: 10.1029/2011GC003875.
542
543 S. Kedar and F. H. Webb. The ocean's seismic hum. Science, 307(5710):682–
544 683, 2005. doi: 10.1126/science.1108380.
545
546 M. Landès, F. Hubans, N. M. Shapiro, A. Paul, and M. Campillo. Origin of deep
547 ocean microseisms by using teleseismic body waves. Journal of Geophysical
548 Research: Solid Earth, 115(B5):B05302, 2010. ISSN 2156-2202. doi:
549 10.1029/2009JB006918.
550
551 E. Larose, P. Roux, M. Campillo, and A. Derode. Fluctuations of correlations
552 and Green's function reconstruction: Role of scattering. Journal of Applied
553 Physics, 103(11):114907, 2008. doi: 10.1063/1.2939267.
554
555 F.-C. Lin and V. C. Tsai. Seismic interferometry with antipodal station pairs.
556 Geophysical Research Letters, 40(17):4609–4613, 2013. ISSN 1944-8007. doi:
557 10.1002/grl.50907.
558
559 F.-C. Lin, V. C. Tsai, B. Schmandt, Z. Duputel, and Z. Zhan. Extracting seismic
560 core phases with array interferometry. Geophysical Research Letters,

40(6):1049–1053, 2013. ISSN 1944-8007. doi: 10.1002/grl.50237.

M. S. Longuet-Higgins. A theory of the origin of microseisms. Philosophical Transactions of the Royal Society of London. Series A, Mathematical and Physical Sciences, 243(857):1–35, 1950. doi: 10.1098/rsta.1950.0012.

K. Nishida. Global propagation of body waves revealed by cross-correlation analysis of seismic hum. Geophysical Research Letters, pages 1–6, 2013. ISSN 1944-8007. doi:10.1002/grl.50269.

K. Nishida and N. Kobayashi. Statistical features of earth's continuous free oscillations. Journal of Geophysical Research : Solid Earth, 104(B12): 28741–28750, 1999. ISSN 2156-2202. doi: 10.1029/1999JB900286.

T. Nissen-Meyer, A. Fournier, and F. Dahlen. A two-dimensional spectral-element method for computing spherical-earth seismograms -1. moment-tensor source. Geophysical Journal International, 168(3):1067–1092, 2007. doi: 10.1111/j.1365-246X.2006.03121.x.

T. Nissen-Meyer, A. Fournier, and F. A. Dahlen. A 2-d spectral-element method for computing spherical-earth seismograms -2. waves in solid-fluid media. Geophysical Journal International, 174(3):873–888, 2008. doi: 10.1111/j.1365-

246X.2008.03813.x.

P. Poli, H. A. Pedersen, and M. Campillo. Emergence of body waves from cross-correlation of short period seismic noise. Geophysical Journal International, 188(2):549–558, 2012a. doi:10.1111/j.1365-246X.2011.05271.x.

P. Poli, M. Campillo, H. Pedersen, and L. W. Group. Body-wave imaging of earth's mantle discontinuities from ambient seismic noise. Science, 338(6110):1063–1065, 2012b. doi: 10.1126/science.1228194.

M. H. Ritzwoller, F.-C. Lin, and W. Shen. Ambient noise tomography with a large seismic array. Comptes Rendus Geoscience, 343:558–570, 2011. doi: 10.1016/j.crte.2011.03.007.

E. Ruigrok, Draganov, D., and Wapenaar, K., Global-scale seismic interferometry: theory and numerical examples: Geophysical Prospecting, Vol. 56, 395-417, 2008. doi:10.1111/j.1365-2478.2008.00697.

E. Ruigrok, X. Campman, and K. Wapenaar. Extraction of p-wave reflections from microseisms. Comptes Rendus Geoscience, 343:512–525, 2011. doi: 10.1016/j.crte.2011.02.006.

K. G. Sabra, P. Gerstoft, P. Roux, W. A. Kuperman, and M. C. Fehler. Surface wave tomography from microseisms in southern california. Geophysical Research Letters, 32(14) :n/a–n/a, 2005a. doi: 10.1029/2005GL023155.

K. G. Sabra, P. Roux, and W. A. Kuperman. Arrival-time structure of the time-averaged ambient noise cross-correlation function in an oceanic waveguide. The Journal of the Acoustical Society of America, 117(1):164–174, 2005b. doi: 10.1121/1.1835507.

K. G. Sabra, P. Roux, and W. A. Kuperman. Emergence rate of the time-domain Green's function from the ambient noise cross-correlation function. The Journal of the Acoustical Society of America, 118(6):3524–3531, 2005c. doi: 10.1121/1.2109059.

N. M. Shapiro and M. Campillo. Emergence of broadband rayleigh waves from correlations of the ambient seismic noise. Geophysical Research Letters, 31:L07614, 2004. doi: 10.1029/2004GL019491.

N. M. Shapiro, M. Campillo, L. Stehly, and M. Ritzwoller. High-resolution surface-wave tomography from ambient seismic noise. Science, 307(5715):1615–1618, 2005. doi: 10.1126/science.1108339.

R. Snieder, K. Wapenaar, and K. Larner. Spurious multiples in seismic interferometry of primaries. GEOPHYSICS, 71(4):SI111–SI124, 2006. doi: 10.1190/1.2211507.

L. Vinnik. Sources of microseismic p waves. pure and applied geophysics, 103(1):282–289, 1973. ISSN 0033-4553. doi: 10.1007/BF00876404.

Z. Zhan, S. Ni, D. V. Helmberger, and R. W. Clayton. Retrieval of moho-reflected shear wave arrivals from ambient seismic noise. Geophysical Journal International, 182(1):408–420, 2010. ISSN 1365-246X. doi: 10.1111/j.1365-246X.2010.04625.x.

**FIGURES CAPTIONS:**

**Figure 1.** Map of the network used in this study (see Appendix for details). Triangles, location of the 420 seismic stations; stars, earthquakes (Mw >5.5) that corresponds to HCDs.

**Figure 2**. (a) Synthetic Green's function in the PREM model with a dominant period of 40 s. (b) Correlations stack over the whole year, filtered in 25 s to 100 s period bands, and sorted as functions of inter-station distance with a bin size of 0.1°. Color boxes, area used for the 2D correlations over each day: P (red), PcP (yellow), ScS (green), PKP (orange), S and SS (black) and P'P'df (blue). (c) Detail of the P-PcP waves in the 5-s to 10-s period band.

**Figure 3.** (a) Daily cumulative seismic moment (m0) for the year 2008. (b) Cumulative microseim excitation at 7 s from ocean wave-wave interactions modulated by bathymetry (global summation). (c) Two-dimensional correlation of the daily P (red) and PcP (yellow) waves at the short period. (d) Two-dimensional correlations of the daily global section with the year-stacked global section at the long period and for the different phases. Vertical gray lines, the HCDs.

**Figure 4.** (a) Global section stacked for the 336 LCDs of the year, and (b) for the 30 HCDs (Figure 3, vertical lines). (c) Synthetic section from a 40-s dominant period vertical source in a spherical Earth, using PREM. (d) Cross-correlation of a 2-day-long synthetic coda in the same model.

**Figure 5.** Map of the two dense arrays: LAPNET (Finland) and FNET (Japan). Blue triangles, positions of the stations; white line, great circle that crosses these two arrays; orange patches, two first endfire lobes (two bounces) for the mantle P-wave at 7-s for these two arrays; stars, earthquakes (Mw > 5.5) that correspond to the HCDs; yellow stars, as related to Figure 8.

**Figure 6.** Correlation between LAPNET and FNET arrays sorted as a function of distance. (a-c) At long period. (d-f) At short period. Red lines, theoretical travel-times using PREM. (a, d), Year stack; (b, e), HCDs; (c, f), LCDs. Yellow arrows indicate some spurious phases in the HCD stack.

**Figure 7.** Correlation stacks using theoretical arrival times from PREM and between FNET and LAPNET. Red line, the year stack; gray line, the HCD stack; green line, the LCD stack. Vertical dashed lines, theoretical arrival time for each phase (PREM). Left panels show the waveforms. Right panels show the corresponding envelopes. (a) Short period P. (b) Short period PcP. (c) Long period S. (d) Long period SS. (e) Long period P'P'df.

682

683 **Figure 8.** (a) Daily cumulative seismic moment (m0) for the year 2008. (b)
684 Daily cumulative microseim excitation at 7 s from the ocean wave–wave
685 interaction modulate by bathymetry. Green, global summation; gray,
686 summation limited to P-wave endfire areas. (c) Two-dimensional correlation of
687 daily P-PcP waves at the short period. (d) Two-dimensional correlations of
688 daily global section with the year-stacked global section at the long period
689 and for different phases. Vertical gray lines, HCDs that remain for this
690 dataset.

691

692 **Figure 9.** Comparison between the P'P'df phases reconstructed the day of
693 events 1 (black) and 2 (gray). Top panel: waveforms; bottom panel:
694 corresponding envelopes; vertical dash line, theoretical arrival time given by
695 PREM.

696

## Appendix

Table A1 shows the different networks used for the present study, with a brief description and the number of station actually selected. Except for the FNET and LAPNET data, all of the waveforms were downloaded using PYTHON request protocols: obspy.iris and obspy.arclink packages.

719 **Table A1.**

| Identifier | Description | Stations selected (n) |
|---|---|---|
| AI | Antarctic Seismographic Argentinean Italian Network | 3 |
| AK | Alaska Regional Network | 30 |
| BO | Bosai-Ken Network (FNET, NIED) | 40 |
| CN | Canadian National Seismograph Network | 13 |
| CU | Caribbean Network (USGS) | 8 |
| G | GEOSCOPE | 21 |
| GE | GEOFON | 20 |
| GT | Global Telemetered Seismograph Network (USAF/USGS) | 6 |
| IC | New China Digital Seismograph Network | 9 |
| II | Global Seismograph Network (GSN-IRIS/IDA) | 34 |
| IU | Global Seismograph Network (GSN-IRIS/USGS) | 60 |
| MN | MEDNET Project | 12 |
| PS | Pacific21 | 6 |
| TA | USArray Transportable Array (NSF EarthScope Project) | 42 |
| TW | Broadband Array in Taiwan for Seismology | 7 |
| X4 | ASCENT | 30 |
| XK | LAPNET | 41 |
| ZL | Sierras Pampeanas | 37 |

720

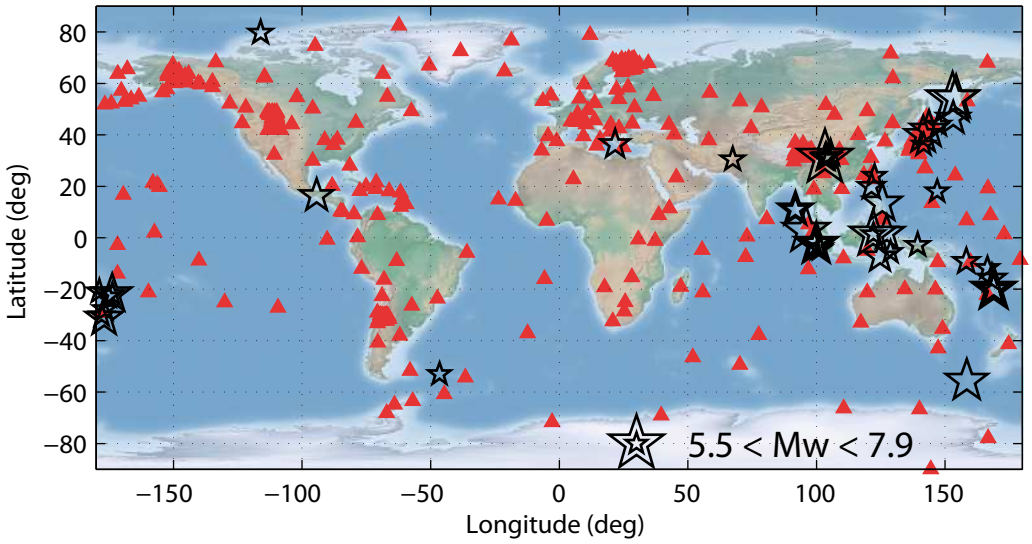
80
60
40
20
0
−20
−40
−60
−80
Latitude (deg)
−150
−100
−50
0
50
100
150
Longitude (deg)
5.5 < Mw < 7.9

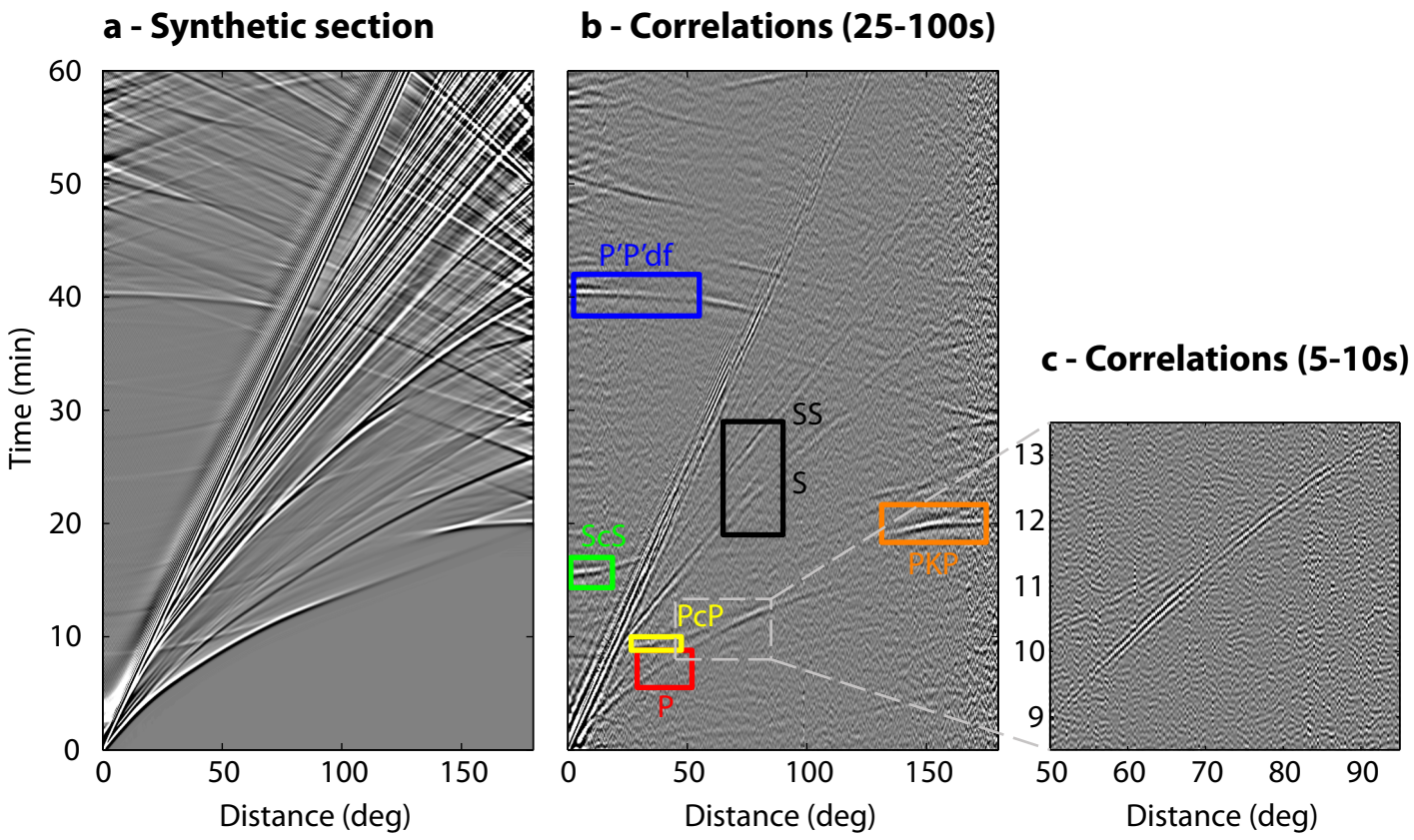
a - Synthetic section
b - Correlations (25-100s)
c - Correlations (5-10s)
Time (min)
Distance (deg)
Distance (deg)
Distance (deg)
P'P'df
SS
S
ScS
PKP
PcP
P

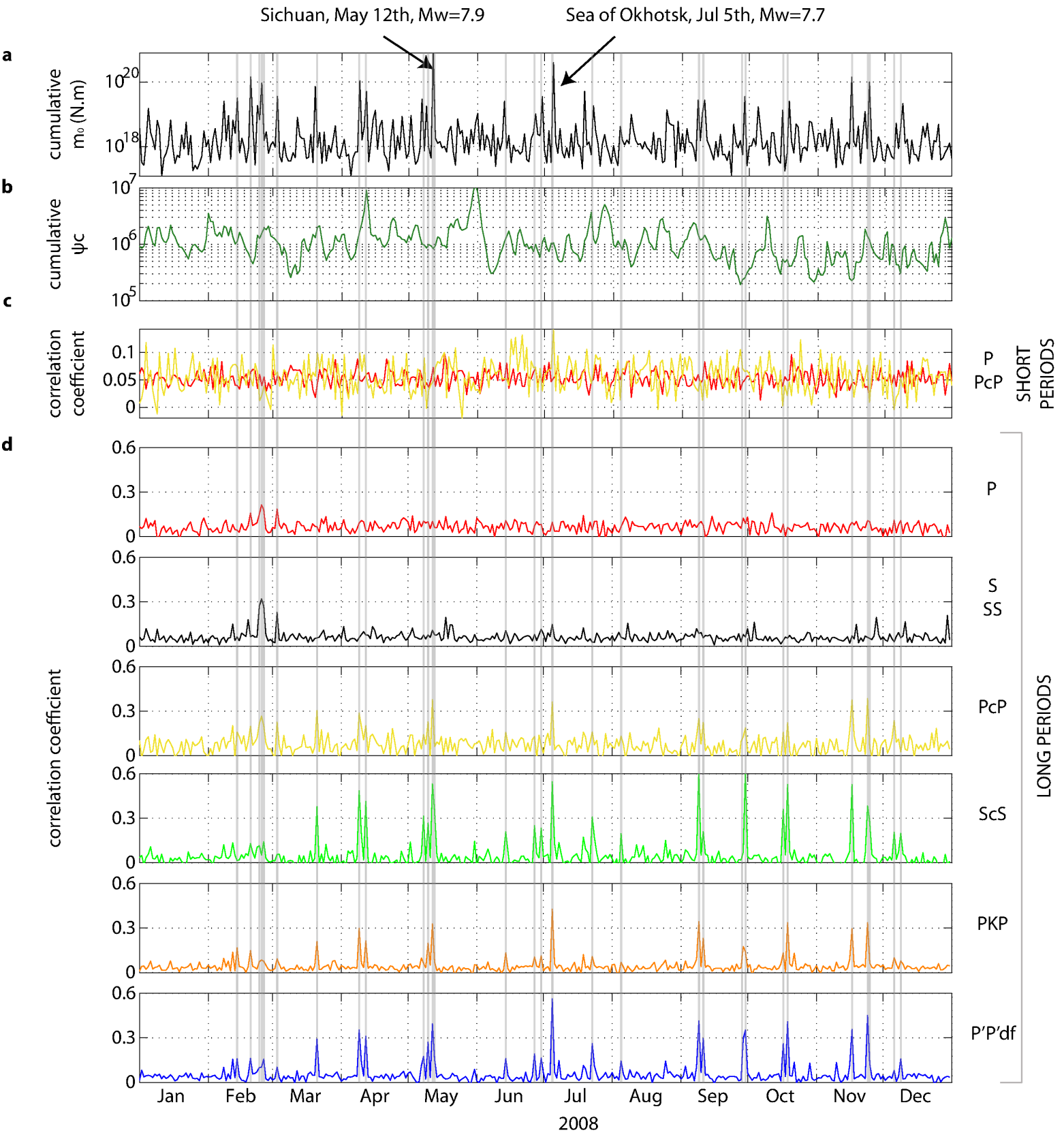
Sichuan, May 12th, Mw=7.9
Sea of Okhotsk, Jul 5th, Mw=7.7
a
cumulative m₀ (N.m)
10^20
10^18
b
cumulative ψc
10^7
10^6
10^5
c
correlation coefficient
0.1
0.05
0
P
PcP
SHORT PERIODS
d
correlation coefficient
0.6
0.3
0
P
S
SS
PcP
ScS
PKP
P'P'df
LONG PERIODS
Jan
Feb
Mar
Apr
May
Jun
Jul
Aug
Sep
Oct
Nov
Dec
2008

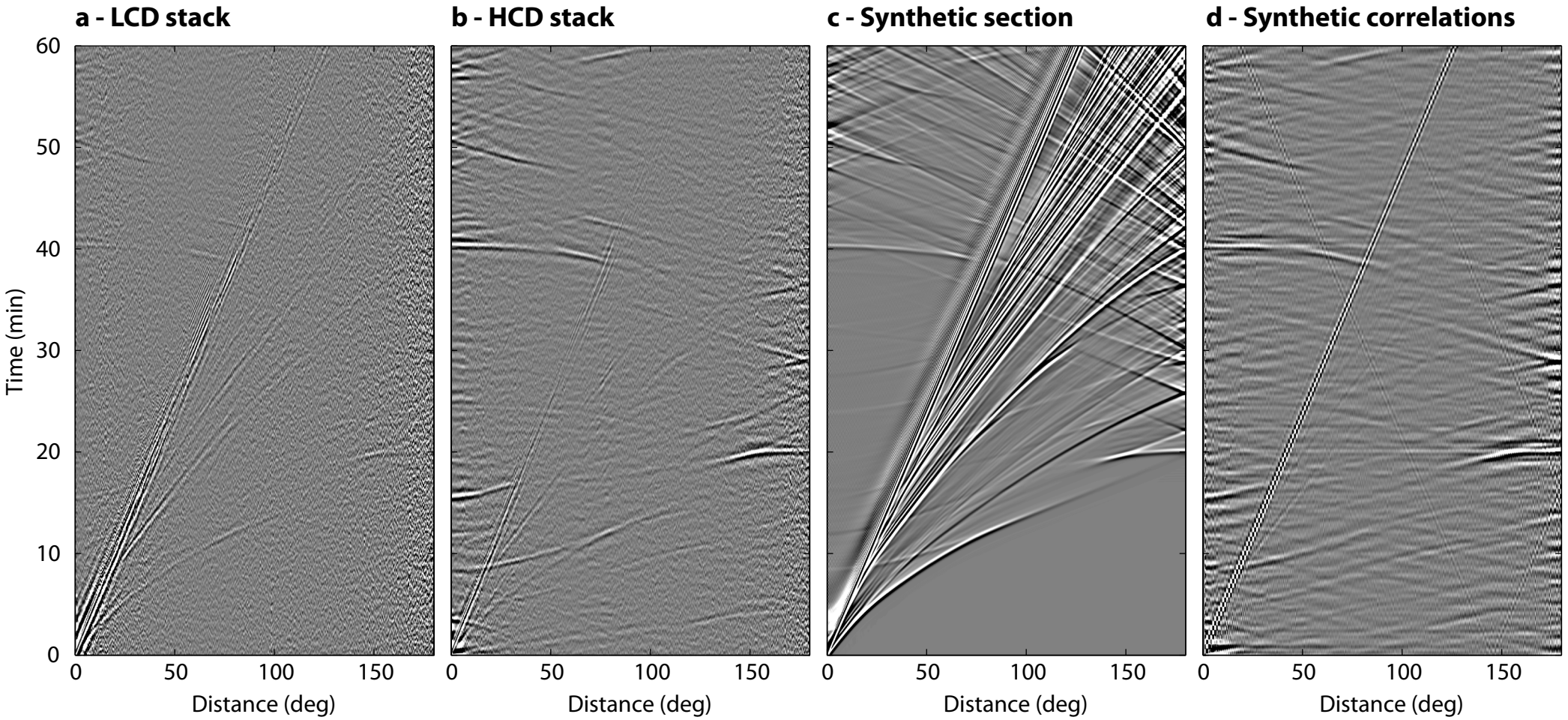
a - LCD stack
b - HCD stack
c - Synthetic section
d - Synthetic correlations
Time (min)
0
10
20
30
40
50
60
0
50
100
150
Distance (deg)

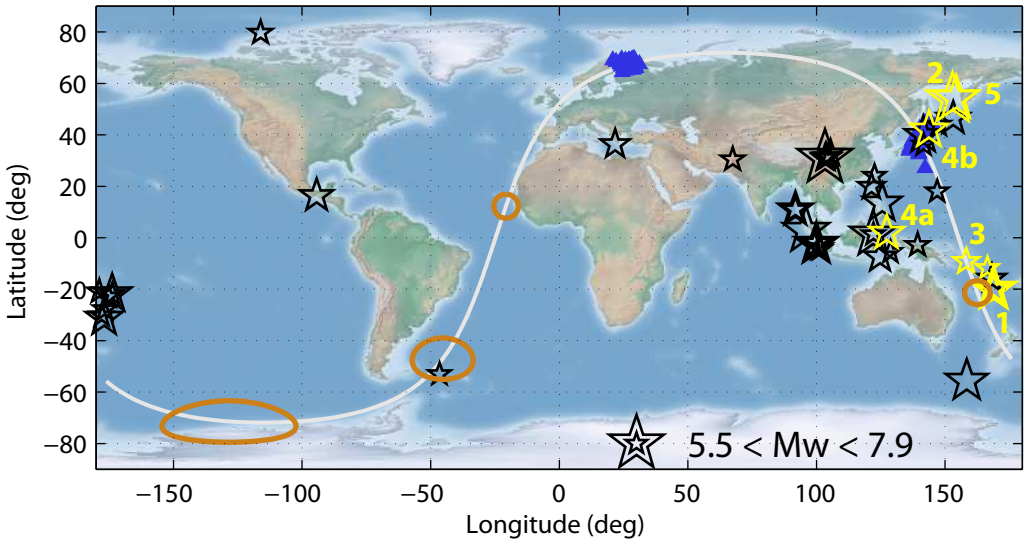
80
60
40
20
0
−20
−40
−60
−80
Latitude (deg)
−150
−100
−50
0
50
100
150
Longitude (deg)
2
5
4b
4a
3
1
5.5 < Mw < 7.9

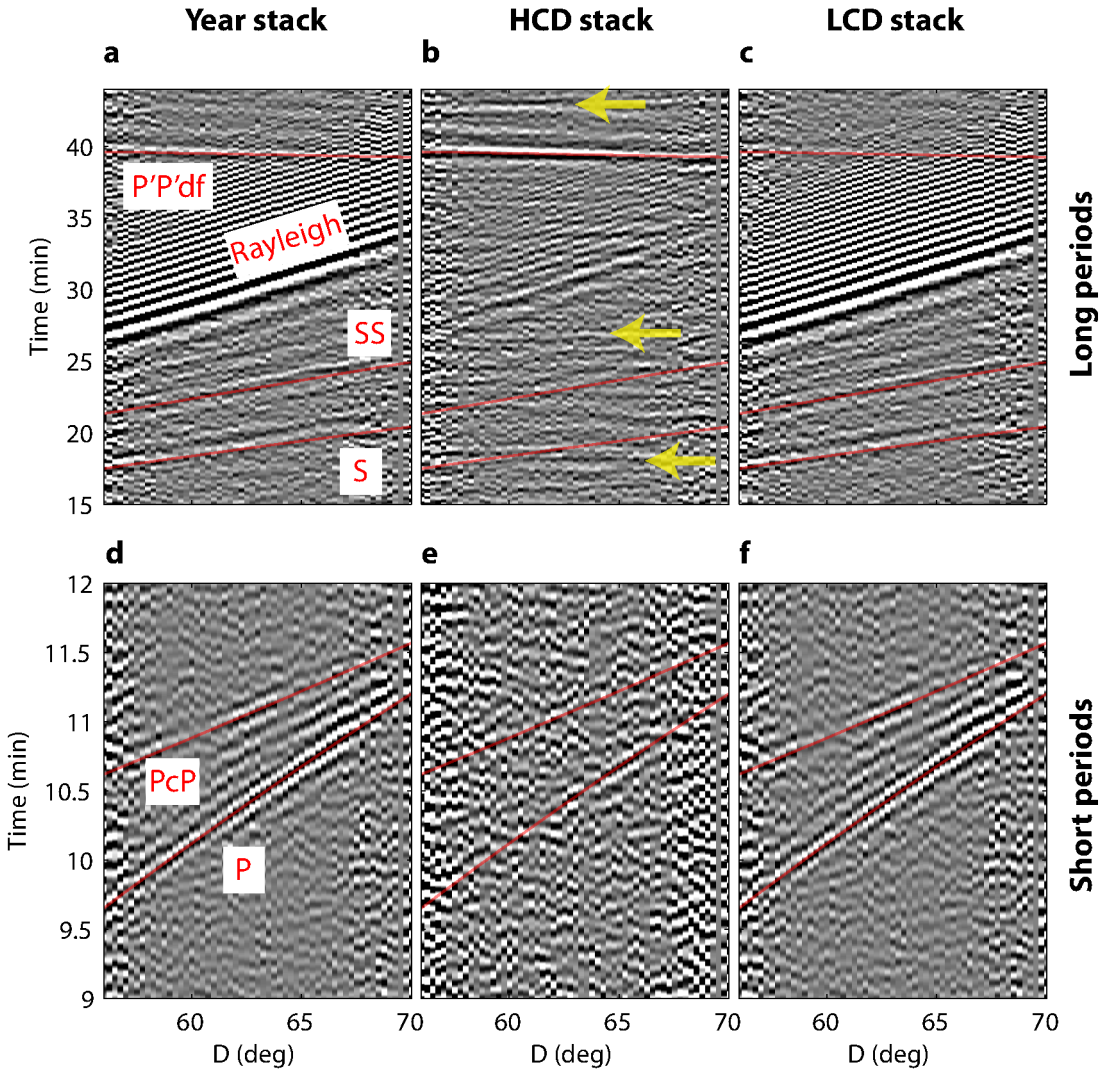
Year stack
HCD stack
LCD stack
a
b
c
d
e
f
P'P'df
Rayleigh
SS
S
PcP
P
Time (min)
40
35
30
25
20
15
12
11.5
11
10.5
10
9.5
9
60
65
70
D (deg)
Long periods
Short periods

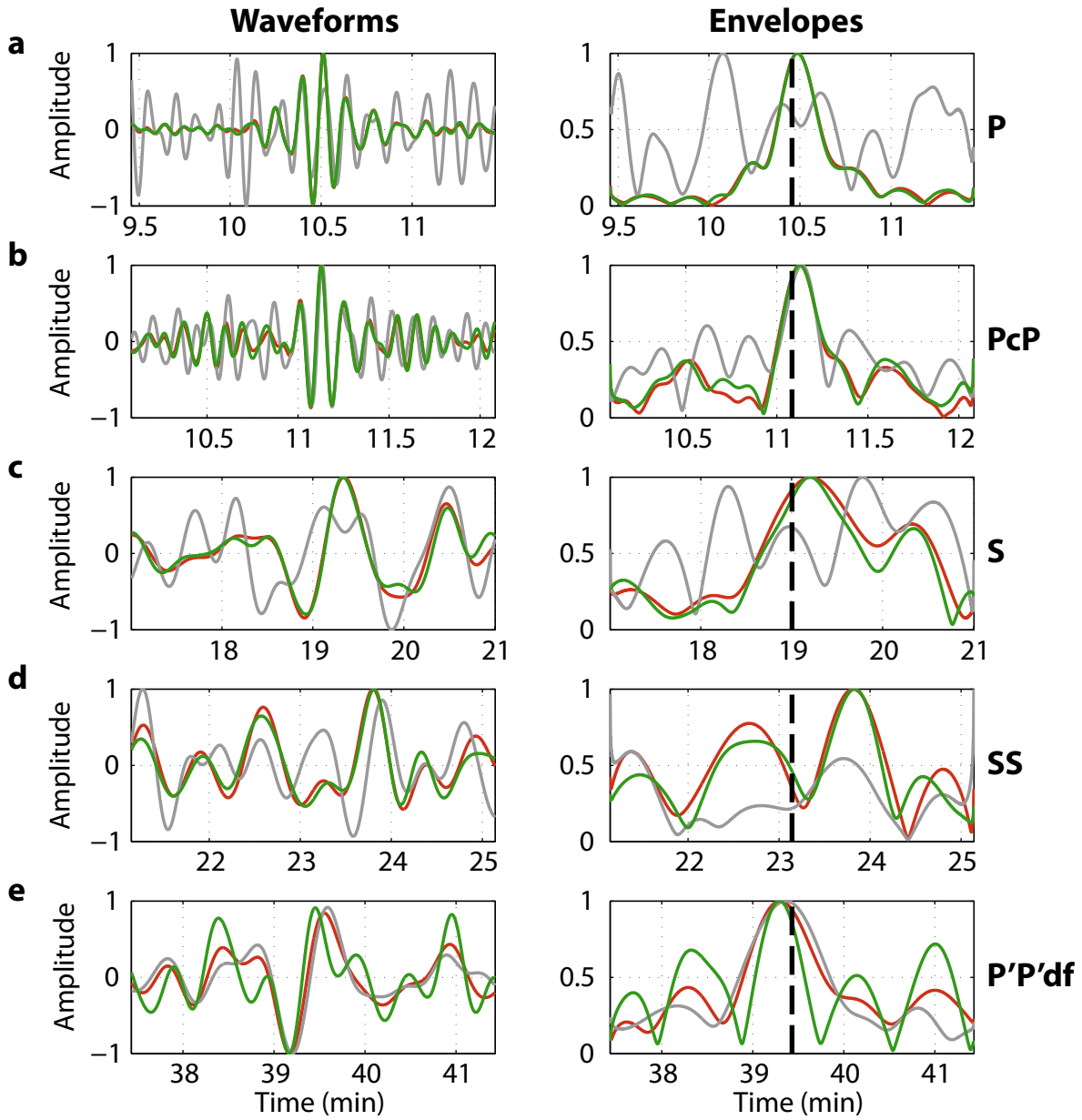
Waveforms
Envelopes
a
b
c
d
e
Amplitude
P
PcP
S
SS
P'P'df
Time (min)

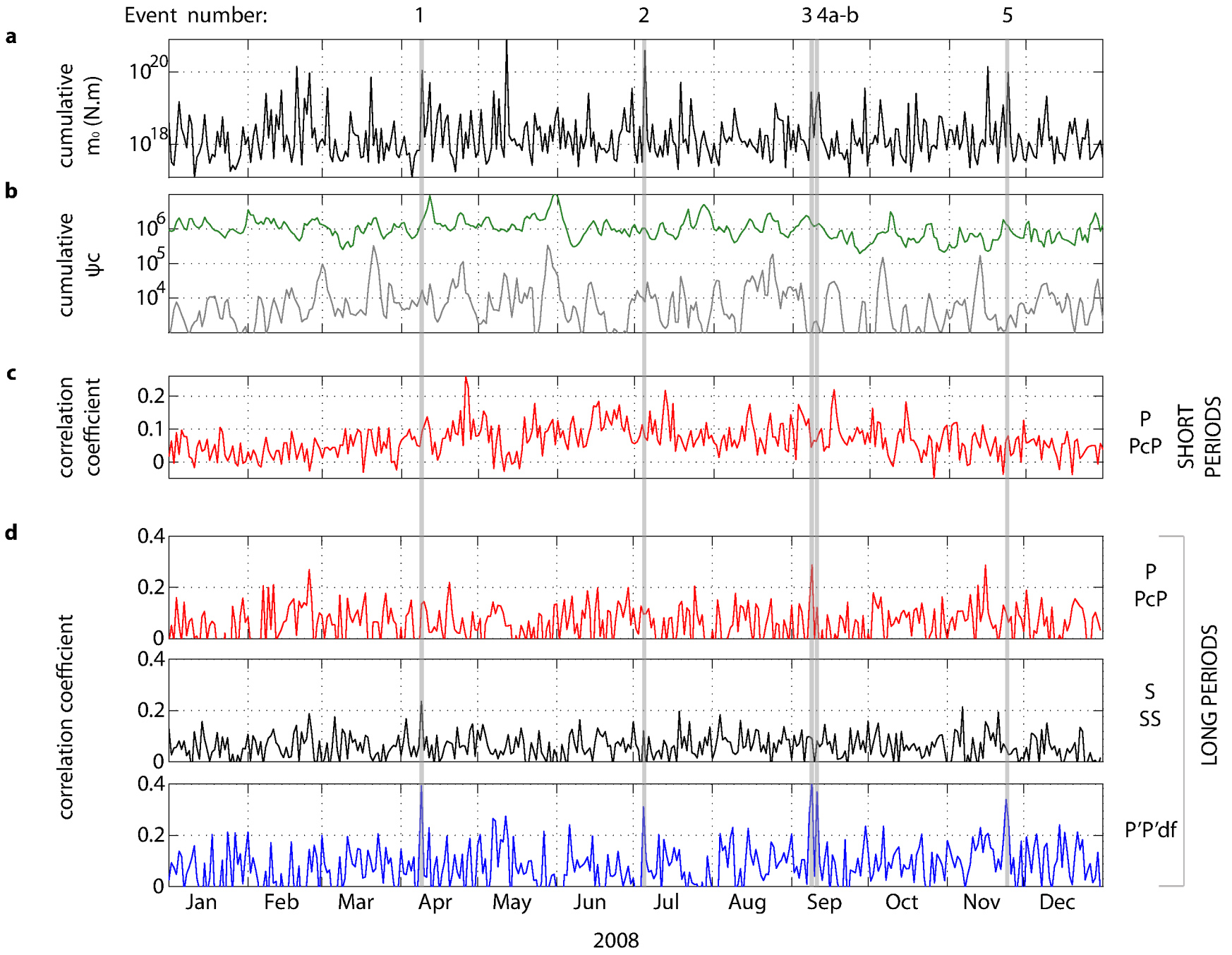
Event number:
1
2
3 4a-b
5
a
cumulative m₀ (N.m)
10^20
10^18
b
cumulative ψc
10^6
10^5
10^4
c
correlation coefficient
0.2
0.1
0
P
PcP
SHORT PERIODS
d
correlation coefficient
0.4
0.2
0
P
PcP
S
SS
P'P'df
LONG PERIODS
Jan
Feb
Mar
Apr
May
Jun
Jul
Aug
Sep
Oct
Nov
Dec
2008

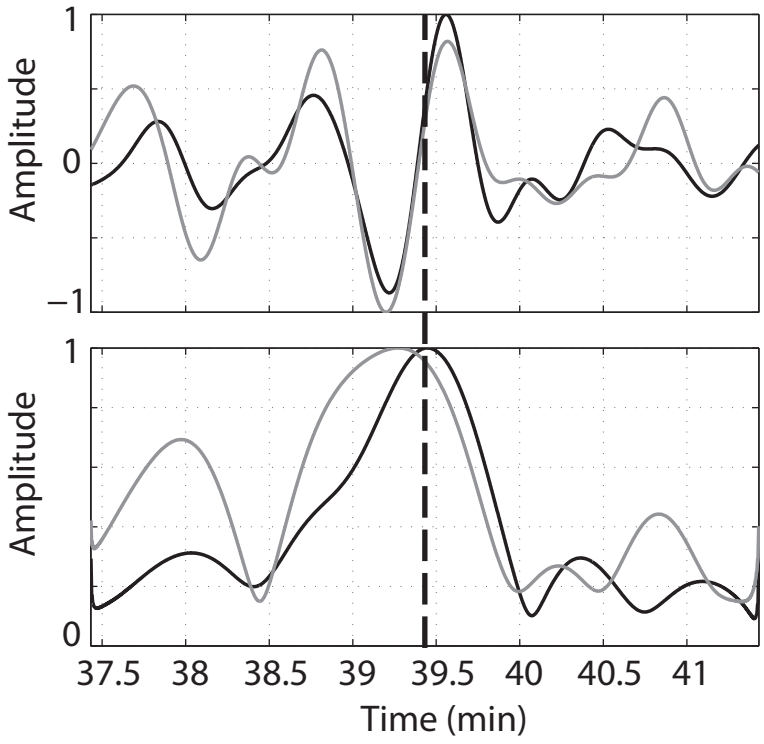
1
0
−1
Amplitude
1
0
Amplitude
37.5
38
38.5
39
39.5
40
40.5
41
Time (min)